Observation and analysis on free surface air entrainment and single bubble movement in supercritical open channel flow

Wangru Wei[1], Weilin Xu[2], Jun Deng[3], Yakun Guo[4]

Abstract: There has been little study on the microscopic bubble entrainment and diffusion process on the high-speed self-aerated flows although the problem under investigation is theoretically important and has important engineering application. This study presents an experimental investigation on visual processes of free surface air entrainment and single bubble diffusion in supercritical open channel flows. The typical surface deformation, single air bubble rising and penetration are recorded using a high-speed camera system. Results show that for a single bubble formation process, surface entrapment development and bubble entrainment through a deformation evolution underneath the free surface are the two main features. The shape variation of local surface deformation with time follows an identical power law for different bubble size generations. The entrained bubble size depends on both size scale and shape of entrapped free surface. As the single bubble moves downstream, its longitudinal velocity is approximately the same as that of water flow surrounded it, while its vertical velocity for rising and penetration increases with the increase of the water flow velocity. An empirical-linear relationship for the bubble rising and penetration velocity with water flow velocity is obtained. This study demonstrates that the microscopic bubble movement can improve the self-aeration prediction in the open channel flow

[1]Lecturer, State Key Laboratory of Hydraulic and Mountain River Engineering, Sichuan University, Chengdu, China, 610065. E-mail: weiwangru@scu.edu.cn
[2] Professor, State Key Laboratory of Hydraulic and Mountain River Engineering, Sichuan University, Chengdu, China, 610065 (Corresponding author). E-mail: xuwl@scu.edu.cn
[3]Professor, State Key Laboratory of Hydraulic and Mountain River Engineering, Sichuan University, Chengdu, China, 610065. E-mail: djhao2002@scu.edu.cn
[4]Professor, Faculty of Engineering & Informatics, University of Bradford, Bradford, BD7 1DP, UK. (Corresponding author). Email: y.guo16@bradford.ac.uk

and advance the knowledge of our understanding of the macroscopic and microscopic air–water properties in hydraulic engineering.

Keywords: free surface; air entrainment; air bubble; open channel flow

Introduction

Air entrainment takes place naturally through free surface of high-speed flows in hydraulic engineering, as shown in Fig. 1. Vertical continuous air concentration profile is found with different shapes as mean void fraction increases in flow direction (Straub and Anderson 1958). This conveyed air transported with water greatly increases the bulk volume of the flow, greatly affecting the hydraulic structure design (Falvey 1980; Ervine 1998). Such air entrained in water flow reduces the air-water mixture density and can change the energy dissipation downstream (Xu et al. 2004; Wei et al. 2013; Guo 2014; Chanson 2015). The presence of air bubbles near structure walls can reduce or prevent cavitation damage caused by high-speed flows (Wilhelms et al. 2005; Frizell et al. 2013; Xu et al. 2015). In addition, water quality is affected by the excess of air introduced into water (Gameson 1957; Bung and Valero 2018). Moreover, air bubbles can alter flow turbulence properties, boundary layer thickness (Castro-Orgaz and Hager 2010; Castro-Orgaz 2012), shear stress, and free surface momentum transfer (Wang et al. 1990; Guo et al. 1999; Yang and Dou 2010; Balachandar and Eaton 2010).

The mechanism of the air entrainment is identified with primary causative influence from free surface turbulence, where an accepted threshold of the intensity of eddy turbulence is surpassed (Pagliara et al. 2011; Pfister and Hager 2011; Bung 2013). The deformation of a local free surface is considered as the direct “carrier”, resulting in individual bubbles entrained into the water flow. Volkart (1980) observed the swelling of the free water surface, indicating that air bubble entrainment might be caused by water droplets falling back to the free surface. Rein (1998) applied turbulent vortices theory to analyze the air bubble entrainment generation. However, his theory was not supported by the laboratory investigation (Straub and Anderson 1958). The air bubble size distribution using these methods differ from that measured and observed (Pumphrey and Bjørnøl 1989; Medwin et al. 1990; Oguz and Prosperetti 1990; Cole and Liow 2004). Brocchini and Peregrine (2001) described a wide range of free surface deformations and investigated the effects of gravity, surface tension, and turbulence kinetics on free surface breakup and bubbling. Valero and Bung (2016, 2018a) proposed a linkage between free surface distortion and the perturbation breakup in high speed flows, and established a kinematic and dynamic consideration. This highlighted the importance of microscopic surface shape and size scale in the generation of the air–water mixture.

So far, the process of air entrainment in high-speed free surface flows has not been fully understood and it is difficult to accurately predict macroscopic air–water properties, such as mixture flow depth, air content, and air concentration distribution in hydraulic engineering. From the point of view of microscopic level, air–water mixture across the flow depth is mainly characterized by the bubble motion in water. The vertical motion, expressed by bubble rising velocity (Haberman and Morton 1954), is important for the air–water diffusion process in open channel flows. Comolet (1979) developed a theory for describing the rising velocity for different bubble size spectrum in still water. However, the situation in flowing water could be very different. Once entrained into the flowing water, individual air bubbles move longitudinally and vertically in two dimensional diffusions, which is more complicated than that in still water (Culligan et al. 2006). This complex flow phenomenon is caused by the interactions of inertia, drag, buoyancy and turbulent eddy diffusion, and their effects on coalescence and break-up in the turbulent flow. The description of bubble diffusion behavior could affect the prediction of the aeration development downstream and the cross-sectional distribution of the air concentration (Falvey and Ervine 1988). Toombes and Chanson (2007) and Felder and Chanson (2014) applied the intrusive conductivity probes to detect the air-water interface transfer, while the bubble rising velocity was inferred indirectly to describe the time-averaged air–water diffusion behaviors in two–phase flows (Chanson 1993; Kramer 2004). The hypothetical inferences make the basic diffusion theory of two–phase flows be limited to specific applications (Wood 1984; Chanson and Toombes 2002; Valero and Bung 2018b). Until now, there is little information on the temporal and spatial movements of air bubbles around the inception aeration area in high-speed flows. Air bubble behaviors in the air–water mixture process from the visual observation on the microscopic movements within free-surface open channel flows are not yet fully understood.

Given limited information and previous shortcomings of analysis, the aim of the present study is to provide new insights into potential consequences of free surface air entrainment generation and bubble diffusion in open channel flows. To this end, a high-speed camera system is used to record the visual processes of entrained bubble generation and movement within supercritical free surface flows. Recoded local free surface entrapment and bubble entrainment images are used to analyze the shape and size of air bubbles. The movement properties of air bubbles, such as rising and penetration in the water flow are obtained for a wide range of bubble size. Furthermore, the present investigation analyzes the effect of bubble diffusion relationship on the aeration development prediction in high speed open channel flows.

Experimental Design and Conditions

Laboratory experiments are conducted to investigate the air entrainment and single bubble movement in open channel flows. Experimental flume is a rectangular glass channel having the dimension of 8.6 m (long) × 0.4 m (wide) × 0.6 m (high), as shown in Fig. 2. Water enters into a horizontal channel from the inlet tank and then flows through a crest transition section connected to a straight channel downstream (see Fig. 2(b)). The straight channel slope α is kept constant of 36° for all tests to enhance the flow acceleration and air entrainment occurrence in the experiments. Five water flow discharges, namely Q = 0.109 m^3/s, 0.117 m^3/s, 0.119 m^3/s, 0.131 m^3/s and 0.137 m^3/s, are conducted. The flow discharge is measured by a rectangular-thin-weir downstream. Given the extremely rapid variation in shape of the free surface and air bubbles (on the order of 1 – 10 ms), and the relevant sub-millimeter length scale (Strotos et al. 2016), a high-speed camera system is used to capture and record the entire process of free surface deformation and single bubble movement. The high-speed camera-based data acquisition system consists of a high-speed video camera (MotionPro Y3-class, Integrated Design Tools Inc., USA) with a Nikkor lens, transferring captured image signals to a computer. The shooting scope is 30 × 12 cm^2, with an image area of 1280 × 324 pixels. All the free surface bubble entrainment and bubble movements for each case are captured and analyzed in this shooting scope. The camera is set with an adjustment fixing mechanism to measure free surface flow along the 30 cm streamwise length. The lens is adjusted to the same elevation as the free water surface, and is perpendicular to the sidewall of channel. High-speed images are taken at 3000 frames per second with an exposure time of 0.0003 s and a sample duration of 3 s. The focus plane is set approximately 3 mm inside from the sidewall. A uniform lighting is provided by an 18 W constant current LED without stroboscopic pulse from the opposite side of the channel, which ensures that a clear luminous beam to the camera through the free water surface is achieved. The stable illumination facilitates the capture and determination of the air–water interface position.

The two-dimensional air concentration distribution at the central line of tested channel is measured using a phase-detection needle probe (CQY-Z8a Measurement Instrument, China, Wei et al. 2016). The tip consists of an internal platinum needle with a diameter 0.05 mm, and the two tips are aligned in the flow streamwise direction with a distance 9.28 mm. The sampling rate is set as 200 kHz with a sampling duration of 10 s. It should be noted that the aeration property difference between the central and near sidewall regions cannot be avoided due to the sidewall effect on flow velocity characteristics. Thus, the present experimental measurement aims to explore the general aeration intensity and corresponds to classical air-water mixture experiments. Typical air concentration profiles for various flow conditions are plotted in Fig. 3, which are in good agreement with characteristic self-aerated flows in open channel (Hager 1991; Chanson 1997). The average air concentration at flow cross-section C_{mean} is deduced by integrating over the flow depth between channel bottom and the mixture flow surface h_{90} where local concentration is $C = 90\%$

$$C_{\mathbf{mean}} = \frac{1}{h_{90}} \int_0^{h_{90}} C \ \mathrm{d}h \tag{1}$$

The characterized clear water depth h_{w} is obtained as:

$$h_{\mathbf{w}} = h_{90} \cdot (1 - C_{\mathbf{mean}}) \tag{2}$$

The average flow velocity is then calculated as:

$$V = \frac{Q}{W \cdot h_w} \tag{3}$$

where W = the channel width. Detailed experimental conditions are listed in Table 1. The aeration expression of the observation region refers to all tested conditions with C_{mean} = 5.6% – 7.9%. This indicates that the free surface air entrainment is relatively weak and the aeration layer at the free surface region is thin with a large clear water layer at the flow cross-section. Under these conditions, the free surface deformation and air–water mixture can be moderated for visual observation. The average free surface velocity V_{fs} is provided to show the surrounding velocity in the air-water mixture area. Considering the thin aeration layer in each case, the V_{fs} is obtained from the average value of air-water velocities over the air-water mixture layer.

For the characterized dimensionless flow parameters, Reynolds number is defined as $Re = Vh_w/\upsilon$, and Weber number We is defined as $We = \rho V^2 h_w/\sigma$, where υ = the kinematic viscosity, ρ = water density and σ = the surface tension. Previous studies showed that the scale effect of air concentrations and bubble transport in aerated open channel flows was limited provided that Re and $We^{0.5}$ were larger than 1.0×10^5 and 110, respectively (Boes and Hager 2003; Pfister and Chanson 2014). For the experimental conditions carried out in this study, the minimal values of Re and $We^{0.5}$ are 2.73×10^5 and 124.48, respectively, demonstrating that the scale effect can be neglected.

A series of instantaneous images are recorded continuously. The two-dimensional air–water interface profile is determined on the basis of the difference in luminance between air and water (Bung 2013; Besagni et al. 2016). A ruler is placed above the free surface inside the flume with the identical slope of channel bottom and is used as the reference calibration of conversion factor between pixels and model millimeter scales. The camera is appropriately adjusted to focus on the ruler plane. The pixels have a horizontal and vertical resolution of 10^{-1} mm. The raw movies are used to identify the bubble entrainment and generation caused by local free surface deformation based on a time series of air–water interface evolution. This ensures that the specific entrained bubble is linked to the spatial and temporal behaviors of corresponding deformed free surface. Owing to the hollow-shape of local two-dimensional free surface, as shown in Fig. 4, the length and depth of entrapped deformation are extracted to describe the free surface deformation quantitatively. The local air-water interface is detected to determine the surface edge. Because the entrapped shape is not symmetrical, the depth y of an entrapped part is defined as the distance between apex and the mid-point of the length L.

For the individual bubble movement of each case, the specific position is tracked per time interval. It is difficult to avoid the air-water interface transverse movement around the focus plane due to the random occurrence of forward and backward movement in the transverse direction, but it is assumed that such movement is small in the present 30 cm length shooting scope. The weak aeration level near the free surface and high sampling frequency can reduce the effect of different planes in the determination of a specific bubble entrainment. Because the shape of air bubbles is irregular, individual bubble size is considered as a spherical particle with the equivalent diameter being d_{ab} for the convenience of description and analysis. Although there are many individual air bubbles in such low air concentration region, the amount of air bubble entrainment case with full and clear free surface deformation process is limited. This is mainly due to the fact that the disturbing surroundings are complicated, such as adjacent free surface movements and intruding following air bubbles. To better understand the bubble entrainment at the free water surface and bubble movement, the bubble size recorded and analyzed has a range from 1 mm to 10 mm for the flow conditions investigated.

Results and Discussions

Free Surface Air Entrainment and Bubble Generation

Fig. 5 shows a typical time series of images from a visual process of free surface entrapment and bubble entrainment for V = 5.5 m/s in which grey-dark shade represents air while white color represents water. Initially, the free surface is relatively smooth and flat with a wave-like shape (t = 0.0 – 2.1 ms). When a disturbance towards inside the water flow acts on the surface, an "entrapped air" appears (t = 2.4 – 4.5 ms). The free surface is clearly higher than the entrapped air center and the surface becomes unstable and shrank at a middle position (t = 4.8 – 6.0 ms). This entrapment continues to develop and eventually an air bubble is formed and entrained into water (t = 6.3 – 7.2 ms). The determination of an individual bubble is dependent on the initial appearance with a visual and continuous air–water interface below the free surface. For this process at t = 7.2 ms, the air–water interface around approximately spherical boundary of this bubble can be seen clearly in the image, separating from the water surface. In this process, the air bubble size of the equivalent diameter is about d_{ab} = 2.5 mm.

The visual process shows that air bubble entrainment in the open channel flow is the evolution of free surface entrapment deformation. Fig. 6 is the observed (a) and the schematic diagram (b), to show the process of free surface air entrainment. Such air entrainment at free surface has two stages: development and entrainment. This process accompanies with the size variations of deformed surface including the distance length L between the two sides of entrapment surface and depth y of entrapment shape. The ratio of L/y describes the entrapment deformation shape. Small L/y represents the deeper penetration of entrapment surface. Initially, the length and depth of a local free surface remain approximately the same. Once the local free surface is disturbed by a vertical fluctuation, such as the turbulence, water droplet, streamwise velocity slip etc., the entrapment shape of free surface is generated as the inception of air entrainment process. During the development stage, the entrapment cavity develops with both the length and depth increasing. The value of L/y decreases significantly, indicating that the entrapment cavity penetrates deeper into water. During the entrainment stage, the remarkable feature is the shrink of entrapped free surface, which is considered to be unstable. The entrapped surface at both sides shrinks. Air entrapped in the cavity is entrained as an individual bubble when the entrapped free surface gets enclosed in the shrink deformation process. The increase of y with decrease of L indicates the as the bubble separates from free surface and enters into water, the free surface rebounds and returns back to the inception state.

The above analysis confirms that the air entrainment in open channel flows is resulted from the unstable surface deformation. Because several forces, such as velocity fluctuations, gravity, surface tension and surrounding pressure (Valero 2019), act on the entrapped deformed surface, it is difficult to remain the stable distortion once the entrapment cavity penetrates deeply. Fig. 7 plots 10 air entrainment processes for present 5 flow conditions and two bubble sizes generated for each case. In Fig. 7(a) and (b), the instantaneous development of the entrapment surface in the length direction can be obtained by $v_L' = \mathrm{d}L/\mathrm{d}t$, and the entrapment surface penetrating into the water with an instantaneous velocity v_y', defined as $v_y' = \mathrm{d}L/\mathrm{d}t$. Both of the two velocities are introduced to describe the detailed geometry variation in the unstable shape deformation process. The time mean velocities of $(v_L')_{mean}$ and $(v_y')_{mean}$ are obtained from the visual process of free surface entrapment and bubble entrainment. The fluctuations of v_L' and v_y' show a strong unstable free surface instability. The values of $(v_L')_{mean}$ are mainly greater than that of $(v_y')_{mean}$, indicating that the penetration of entrapment surface into the water is the key feature in the deformation process. The positive and negative mean values of v_L' indicates the length variation of entrapment development depend on specific bubble entrainment cases. Compared with the local free surface mean velocity, both of $(v_L')_{mean}$ and $(v_y')_{mean}$ are generally smaller than V_{fs} on the order of 10% – 20%. In terms of the variation rate of L/y, its development may be expressed as:

$$\frac{\mathrm{d}(L/y)}{\mathrm{d}t} = 6 \cdot (\tanh\frac{t}{t^*} - 1) \tag{4}$$

The regression coefficient of $R^2 = 0.565$. The normalization of Eq. (4) includes t/t^*, where t^* is a referred time scale, suggested as $t^* = 1$ ms in the present conditions. From Eq. (4) follow $\mathrm{d}(L/y)/\mathrm{d}t = -0.216$ at $t = 2$ ms and $\mathrm{d}(L/y)/\mathrm{d}t = -0.004$ at $t = 4$ ms, respectively. The data trend indicates that the entrapment shape variation underneath the surface in the bubble entrainment process depends on the time duration. For time duration smaller than about 4 ms, the L/y is a variable, while it can be considered as a constant for time duration exceeding 4 ms. This is important for the basic theory in which the length and depth scale are the key geometry parameters affecting the kinematics and dynamic analysis of free surface turbulent deformation. For the upstream free surface perturbation analysis (Valero and Bung 2018a), the linear relationship between the length and amplitude of the submerged body can be established for the time duration greater than 4 ms. For shorter time duration of a free surface break-up and air entrainment process, the effect of geometry variation should be further considered.

In Fig. 7(d), T_0 is the total time of the development and entrainment duration. The end of entrainment stage is determined on the basis of the photo frame order in which a single bubble with clear air–water interface all around separates from the surface entrapped it. The rapid decrease in L/y in the initial duration (i.e. $t/T_0 < 0.2$) illustrates that the free-surface deformation develops rapidly. It is seen from Figure 7 that the data in the $t/T_0 < 0.2$ are a bit scatter, which may be ascribed to the fact that the difference of the random disturbance and strong free surface interaction exist during the initial development stage. The variation trend then becomes gradual for the rest of time, i.e. $0.2 < t/T_0 < 1.0$. Fig. 7 also demonstrates that the variation of L/y with dimensionless time for different bubble size is similar. Analysis of the ten bubble generation data shows that the relationship between L/y and t/T_0 follows a power law:

$$L / y = m \cdot (t / T_0)^{-n} \tag{5}$$

Using the experimental data, the coefficient m and exponent n in equation (5) can be determined as 1.6 and 0.5, respectively, with the regression coefficient of $R^2 = 0.912$. Fig. 7 confirms the uniformity of the free surface entrapment deformation and bubble entrainment process.

Be analogy to the previous analysis about the free surface perturbation breakups (Valero and Bung 2016; Valero and Bung 2018a), the ratio of L/y can be used to express the entrapment steepness. Valero and Bung (2018a) deduced that the ratio of length to perturbation amplitude (the radial height above the mean free surface) should be below a limiting steepness for the inception of distortion breakup and the onset of air entrainment. For the deformation shape underneath the mean free surface, they made a hypothesis of $y = 0.5L$ (expressed in the present parameters) for the perturbation geometry as it developed from a vertical velocity fluctuation on the free surface. This is consistent with the entrainment stage of this study where the entrapment shape becomes shrunk with bubble generation. The development stage is a necessary condition for bubble entrainment generation. Whether the bubble is entrained into water is dependent on the entrainment stage in which the entrapment distortion becomes significant within the L/y getting decreased to 2. Analysis shows that the surface deformation corresponds to the turbulence intensity and aeration level in self-aerated open channel flow. The highly aerated area sustains much small. The result demonstrates that the entrapment deformation evolution of free surface in open channel flow is an essential process for the air bubble generation.

Based on the entrapment characteristics of free surface deformation development and air entrainment, the length L_m and depth y_m of the entrapped shape at the end of developing period before the shrink are used as the scale parameters to describe the threshold shape of local surface (i.e. the shape at t = 4.8 ms in Fig. 5). Fig. 8 shows the relation of surface entrapment size scales and the entrained bubble size. Comparing with the entrapped deformation quantitatively, the skew distribution in the $d_{ab} < L_m$ and $d_{ab} < y_m$ regions indicates that most air bubble equivalent sizes are smaller than the deformation size at both the longitudinal and lateral directions. Moreover, it is seen from Figure 8 that the finally formed air bubble size ranges between 0.2 and 2 times of the final deformation size for the parameter ranges tested, that is, $0.2L_m < d_{ab} < 2L_m$, and $0.2y_m < d_{ab} < 2y_m$. This is owing to the shrink feature of free surface entrapment deformation before the bubble entrainment. Both the disturbance effect and the enclosed position seem to be random and unpredictable. On the other hand, with the increase of entrained bubble size, the corresponding ranges of L_m and y_m decrease. For example, for small air bubbles ($d_{ab} < 6$ mm), the orders of magnitude of L_m and y_m range from 1 mm to 14 mm and 1 mm to 10 mm, respectively. While for large air bubble ($d_{ab} > 6$ mm), the order of the magnitude of both L_m and y_m changes to 4 mm to 10 mm. These two features demonstrate that the bubble size is affected by the absolute size scale of deformation.

Fig. 9 shows the relationship between L_m/y_m and d_{ab}. It is seen from Fig. 9 that air bubble size depends on the entrapment deformation shape of free surface. In the present experimental observation, most entrapped shapes of free surface have “long-shallow” type with $L_m/y_m > 1.0$. The “short-deep” type of entrapped free surface for $L_m/y_m < 1.0$ occurs mainly for small bubble ($d_{ab} < 6$ mm). For the large bubble generation ($d_{ab} > 6$ mm), the associated value of L_m/y_m is mainly within the range of 1.0 – 1.5. For $L_m/y_m > 1.5$, the entrained bubble size starts to decrease with the increase of L_m/y_m. This means that in addition to the absolute size scale effect, a moderate value of L_m/y_m with a slightly “long-shallow” type favors the generation of the large air bubble in the free surface evolvement process.

To capture the air bubble entrainment process, the local air concentration in the flow needs to be relatively low for the purpose of the visual clear-water. The amount probability of different bubble size is plotted in Fig. 10(a), where the probability of d_{ab} from 1 to 2 mm is represented by the column labeled 1 mm, and column labeled 6 mm represents the total probability of bubble diameter being larger than 6 mm. Note that air bubbles which are smaller than 1 mm are indeed observed, however, the formation process for this size scale cannot be clearly observed due to the experimental shooting limitations. The probability of small air bubbles is greater than that of large bubble. Comparing the present study with the previous intrusive tests on air bubble size distribution in lower aerated region (Chanson 1997), the observed bubble size distribution in this study is more skewed, with a preponderance of small bubble with $d_{ab} < 6$ mm. The values of mean air bubble size d_{mean} for intrusive and visual tests are different, as shown in Fig. 10(b). The ratio γ of intrusive air chord length over visual bubble size can exceed two, which indicates the intrusive results overestimate the individual bubble scale in self-aerated flows. This can be explained as following. Firstly, it should be noted that the minimum bubble size detected by the intrusive measurement depends on the instrument tip diameter and a reasonable sample rate to avoid aliasing (Chanson 2013). The diameter of needle tip should be much smaller than the smallest bubble size in the air-water flow and the sampling rate should be set according to the flow velocity. However, it is difficult to avoid completely the interface aliasing for small bubble detection. Secondly, the intrusive measurement mainly detects the continuous signal of air–water interface in streamwise direction, therefore, it is difficult to distinguish the deformed surface and the individual air bubble in the air–water mixture region, especially for the process containing both entrapment deformation and bubble entrainment. The size L_m of entrapped surface is generally larger than the final size d_{ab} of the entrained air bubble, thus, the probability of enclosed two-surface sides at lower positions near the entrapped apex is much greater than that for higher enclosed positions. Consequently, the entrained bubble properties (e.g. the size and amount probability) depend on both the size scale and the shape of entrapped free surface. The bubble size distribution obtained from the intrusive measurement cannot represent the bubble size characteristics generated from the free surface air entrainment.

Bubble Diffusion in Water Flow

After a single bubble is entrained into water, it moves downstream with water flow. In vertical direction, the air bubble can either rise towards the free surface or penetrate deeply into water, as shown in Fig. 11, in which some images are systematically skipped during this process to reduce the overlap effect of the particles. The bubble movement across this interval period ($\triangle t$) is approximated as linear motion, and the component velocities ΔV_{ax} and ΔV_{ay} are deduced using respectively the longitudinal and vertical centroid displacement over the time interval. Based on the bubble movement and the variation of instantaneous velocity in Fig. 12, ΔV_{ax} and ΔV_{ay} fluctuate around 0 for both rising and penetrating processes in the low-aerated region. Thus, in the present study, this means that the single bubble's diffusion path for weak air–water mixture can be simplified as a linear motion.

Applying a linear approximation to the bubble movement, the streamwise velocity V_{ax}, rising velocity V_{ay} and penetration velocity V_{ay}' can be estimated from the centroid displacement in both streamwise direction Δx and vertical direction Δy over the same observed period. The order of magnitude of individual bubble size ranges from 1 mm to 10 mm. The characteristic velocities of different bubble sizes are shown in Fig. 13. In the streamwise direction, V_{ax} is approximately the same as the free surface velocity across the range of the bubble size, indicating that the following behavior of bubble moved with water flow downstream is well performed. For the time average process, there is no prominent slipping between single entrained bubbles and the flowing free surface of water bulk. In the vertical direction, the V_{ay} and V_{ay}' generally range from 0.01 m/s to 0.50 m/s. For small bubble size (d_{ab} < 6 mm), the vertical velocity has a wider range (0.01 m/s to 0.50 m/s), while for larger bubble size (d_{ab} > 6 mm), the range of vertical velocity becomes narrow (0.10 m/s to 0.50 m/s). Comparing with the effective bubble rising velocity in still water as a function of the bubble size (Haberman and Morton 1954; Falvey 1980), the vertical velocities are mainly smaller across bubble size scales, especially for small air bubble diffusion process.

The transport process of air bubbles in the water flow is a basic issue for the high-speed aerated flow. In hydraulic engineering, the previous analysis on air–water mixture in the open channel flow was normally established based on the indirect hypothesis of air bubble transport (Wood 1991; Chanson 1993; Kramer 2004). The air bubble motion at vertical direction is characterized as the rising velocity $V_r \cdot \cos\alpha$, representing the air phase spilling over the water flow. The value of V_r can be indirectly deduced by continuity theory (Chanson 1993) and diffusion theory (Liang and Wang 1982; Yuan and Xiang 1988) or air profile gradient (Kramer 2004). Fig. 14 shows the average values of bubble rise and penetration velocities ($(V_{ay})_{mean}$, $(V_{ay}')_{mean}$) from the present study of direct observation. In Fig. 14, the average flow velocity V, which can be estimated easily, is used in order to make the results having wide engineering application. It is seen from Fig. 14 that the $(V_{ay})_{mean}$ and $(V_{ay}')_{mean}$ increase with the increase of water flow velocity. The variation trends of $(V_{ay})_{mean}$ and $(V_{ay}')_{mean}$ with V are approximately the same, which can be best fitted as following:

$$(V_{ay})_{\mathbf{mean}} = (V_{ay'})_{\mathbf{mean}} = (0.023 \cdot V + 0.046) \cdot \cos\alpha \tag{6}$$

where the channel slope α is set to reflect the vertical component of bubble motion. Table 2 shows the comparison of the computed values from Eq. (6) with the previous studies. Good agreement in Table 2 indicates that the present relationship can represent the basic bubble motion in free surface air entrainment and air–water mixture development in open channel flows. Moreover, the same variation trends of bubble rising and penetration processes indicate that the two characterized bubble motions should be equally considered.

Application in Hydraulic engineering

For a self-aerated flow on a spillway in hydraulic engineering, the prediction of gradually varied aeration region downstream of the inception location of free surface air entrainment relates to the accurate recognition of detailed air bubble diffusion process. Based on the air phase continuity in an air–water flow along a channel of constant slope, Wood (1991) and Chanson (1993) proposed an equation for the gradual variation of air quantity entrainment along the spillway:

$$\frac{1}{(1-C_e)^2}\cdot\ln\left(\frac{1-C_{\mathbf{mean}}}{C_e-C_{\mathbf{mean}}}\right)-\frac{1}{(1-C_e)\cdot(1-C_{\mathbf{mean}})}=\frac{V_{\mathbf{r}}\cdot\cos\alpha}{V_0}\cdot\frac{x}{d_0}+K_0 \qquad (7)$$

where x = the distance from the self-aeration inception, V_0 and d_0 = the flow velocity and depth at the self-aeration inception, respectively. The coefficient K_0 can be determined as,

$$K_0=\frac{1}{1-C_e}\cdot\left(\frac{1}{1-C_e}\cdot\ln\frac{1}{C_e}-1\right) \qquad (8)$$

where C_e = the cross-sectional averaged air concentration for the uniform air–water mixture flow, which is a function of the channel slope and can be determined by (Hager 1991)

$$C_{\mathbf{e}}=0.75\cdot(\sin\alpha)^{0.75} \qquad (9)$$

Equation (9) is valid for $7.5° \leq \alpha \leq 75°$. As the channel bed slope is easy to determine, in order to obtain the C_{mean} variation along the spillway, the key factor for solving the Eq. (7) is the characterized bubble velocity V_r. So far, little knowledge on V_r has been available, making it difficult to obtain an explicit solution of C_{mean}. However, the value of V_r may be determined empirically from each specific experimental result (Chanson 1993). Assuming that V_0 equal to V in Eq. (6) and applying this in Eq. (7), the C_{mean} can then be solved explicitly. Fig. 15 shows the comparison of the calculated C_{mean} with the prototype Aviemore dam observation (Cain 1978) and laboratory experiment (Xi 1988). Good agreement between the calculated and measured/observed C_{mean} confirms that the microscopic bubble movement obtained from the visual observation in self-aerated open channel flows can accurately predict the air–water two–phase flow and improve the knowledge of the link between the macroscopic and microscopic air–water properties in hydraulic engineering.

The application about the self-aeration development in open channel flows shows that the characteristic bubble velocity is a key parameter in the air-water mixture process. Firstly, the bubble motion process in still fluid is affected by mechanism factors, including inertial, drag, buoyancy, and fluid kinematic viscosity and density (or air concentration). The decrease of air-water mixture density (or increase of air concentration) can lead to a decrease of the single bubble rising velocity (Chanson 1995, Bennen 2005). Secondly, the turbulent eddy transport force is another important factor for the bubble transport process in high velocity turbulent flows (Falvey and Ervine 1988). The increase of flow velocity enhances turbulent shear and eddy transfer, resulting in significant mass exchange across the flow depth. For very high flow aeration in prototype self-aerated flow (Cain 1978), V_r is almost two times greater than that in scale model flows. Although the high velocity of a self-aerated open channel flow can improve the aeration and decrease the entire flow density, the increase of the bubble velocity inferred from the literature and present observation indicates the bubble vertical transfer is mainly determined by the turbulent eddy transport intensity, and the basic relationships Eq. (6) – (9) can give a reasonable results for some prediction applications.

In the present study, the direct observations on the single bubble transport characteristics can be considered as benchmark data for the air-water mixture development in high speed open channel flows. For air-water flows with complex air-water structures, such as bubble clouds and recirculation and local non-hydrostatic pressure condition, the bubble transfer will be influenced by more microscopic interactions (Kobus 1991; Kramer 2005). These complex conditions influence the bubble shape deformation, collision within break-up or coalescence among each other, and slip movement in distorted streamline area, which may result in different performance of bubble motion. Further experiments will be required to investigate the difference of bubble rise velocity between a single bubble and a mixture structure, and to expand the application of air-water diffusion in high speed open channel flows.

Conclusions

This study presents laboratory experimental results on the free surface air entrainment and single bubble diffusion in open channel flows. The visual processes of free surface deformation and bubble movement are recorded by using a high-speed camera system. Based on the recorded detailed shape deformation, the free surface air entrainment and bubble generation are described quantitatively. Moreover, the single bubble movement with water flow and its effect on the air–water mixture development in self-aerated open channel flows are analyzed.

The free surface entrapment can entrain air into water flow depending on the shape deformation evolution. When the entrapment deformation develops significantly, namely penetrating and distorting steeply below the flow surface, air entrainment occurs by creating individual bubble. For different bubble size generations, the present study shows an approximately identical power law for the evolution trend of free surface entrapment deformation. The entrained bubble size is determined by the deformation size scale, entrapment shape and the unstable enclosed position. A moderate long-shallow type of a local entrapped surface with a large deformation size favors the generation of the large air bubble in the free surface evolvement process.

For the single bubble motion in the low aerated area of high speed open channel flows, its streamwise velocity is approximately the same as that of water flow, while the vertical velocity for both rise and penetration is smaller than that of the effective bubble rise velocity in still water. The well correlation between the bubble vertical velocity and the average flow velocity confirms that the individual bubble vertical transfer is mainly determined by the turbulent eddy transport intensity. An empirical relationship between the single bubble motion and average flow velocity is established from this study, which provides reasonable agreement with measurements. This demonstrates that the microscopic bubble motion properties can promote the self-aeration prediction.

The self-aeration is an unstable interaction process among multiple instability forces on the air–water interface. Air diffusion in the turbulent aerated open channel flow is highly affected by the turbulence transportation. The theoretical framework should be of interest on the study on the linkage between the surface deformation and the turbulence intensity in open channel flows. Further experimental studies on complex bubble motion characteristics are required to better interpret air-water mixture process and to expand application in hydraulic engineering.

Data Availability Statement

All data, models, and code generated or used during the study appear in the submitted article.

Acknowledgements: The research reports here is financially supported by National Natural Science Foundation of China (Grant number 51609162), Sichuan Science and Technology Program (Grant number 2019JDTD0007) and the Open funding of the State Key Laboratory of Hydraulics and Mountain River Engineering of Sichuan University (Project No: Skhl1809). Comments made by Reviewers have

greatly improved the quality of the paper.

Notations

C = air concentration;

C_e = average cross-sectional air concentration for uniform air–water mixture flow;

C_{mean} = average cross-sectional air concentration along the spillway;

d = characterized water flow depth;

d_{ab} = equivalent size of single bubble;

d_{mean} = average air bubble size

d_0 = characterized water flow depth at the self-aeration inception;

h = flow depth from the channel bottom;

h_{90} = mixture flow surface level where local concentration is $C = 0.90$;

K_0 = coefficient;

L = length of surface entrapment;

L_m = length of surface entrapment at the end of deformation development period;

m = coefficient;

n = coefficient;

Q = water flow discharge rate;

T_0 = total time of the development and entrainment periods;

t = time;

V = average flow velocity;

V_{ax} = single bubble velocity in streamwise direction;

V_{ay} = single bubble rising velocity at vertical direction;

$(V_{ay})_{mean}$ = average bubble rising velocity at vertical direction;

V_{ay}' = single bubble penetration velocity at vertical direction;

$(V_{ay}')_{mean}$ = average bubble penetration velocity at vertical direction;

V_{fs} = average free surface velocity;

V_r = bubble rising velocity in literature;

V_0 = flow velocity at the self-aeration inception;

v_L' = instantaneous development of the entrapment surface in the length direction;

$(v_L')_{mean}$ = average velocity of entrapment length development;

v_y' = instantaneous velocity of entrapment surface penetration;

$(v_y')_{mean}$ = average velocity of entrapment penetration development;

W = channel width;

x = streamwise direction from the self-aeration inception;

y = depth of surface entrapment;

y_m = depth of surface entrapment at the end of deformation development period;

$\triangle V_{ax}$ = component velocity over the interval period in streamwise direction;

$\triangle V_{ay}$ = component velocity over the interval period in vertical direction;

$\triangle x$ = centroid displacement in streamwise direction;

$\triangle y$ = centroid displacement in vertical direction.

α = channel slope;

γ = ratio of average intrusive air chord length over visual bubble size.

References

Balachandar, S., and Eaton, J. K. (2010). "Turbulent disperse multiphase flow." *Annu. Rev. Fluid Mech.*, 42, 111-133.

Besagni, G., Brazzale, P., Fiocca, A., and Inzoli, F. (2016). "Estimation of bubble size distributions and shapes in two-phase bubble column using image analysis and optical probes." *Flow Meas. & Instrum.*, 52, 190-207.

Boes, R. M., and Hager, W. H. (2003). "Two-phase flow characteristics of stepped spillways." *J. Hydraul. Eng.*, 129 (9), 661-670.

Brennen, C. E. 2005. *Fundamentals of multiphase flows*. California: Cambridge University Press.

Brocchini, M., and Peregrine, D. H. (2001). "The dynamics of strong turbulence at free surfaces. Part 1. Description." *J. Fluid Mech.*, 449(15), 225-254.

Bung, D. B. (2013). "Non-intrusive detection of air–water surface roughness in self-aerated chute flows." *J. Hydraul. Res.*, 51(3), 322-329.

Bung, D. B., and Valero, D. (2018). "Re-aeration on stepped spillways with special consideration of entrained and entrapped air." *Geosciences*, 8(9), 333.

Cain, P. (1978). "*Measurements within self-aerated flow on a large spillway*." Ph.D. thesis, Univ. of Canterbury, New Zealand.

Castro-Orgaz, O., and Hager, W. H. (2010). “Drawdown curve and turbulent boundary layer development for chute flow.” *J. Hydraul. Res.*, 48(5), 591-602.

Castro-Orgaz, O. (2012). “Velocity profile and flow resistance models for developing chute flow.” *J. Hydraul. Eng.*, 136(7), 447-452.

Chanson, H. (1993). “Self-aerated flows on chutes and spillways.” *J. Hydraul. Eng.*, 119(2), 220-243.

Chanson, H. (1995). *Air Bubble Entrainment in Free-Surface Turbulent Flows: Experimental Investigations*. Rep. No. Ch46/95. Brisbane, Australia: University of Queensland.

Chanson H. (1997). “Air bubble entrainment in open channels: Flow structure and bubble size distributions.” *Int. J. Multiphase Flow*, 1997, 23(1), 193-203.

Chanson, H., and Toombes, L. (2002). “Air–water flows down stepped chutes: turbulence and flow structure observations.” *Int. J. Multiph. Flow*, 28(11), 1737-1761.

Chanson, H. (2013). “Hydraulics of aerated flows: qui pro quo?” *J. Hydraul. Res.*, 51(3), 223-243.

Chanson, H. (2015). *Energy dissipation in hydraulic structures*. IAHR Monograph, CRC Press, Taylor & Francis Group, Leiden, the Netherlands.

Cole, D. E., and Liow, J. L. (2004). “Bubble entrapment during water drop impacts.” *Proc. 15th Australasian Fluid Mech. Conf.*, Sydney, 13-17.

Comolet, R. (1979). “Sur le movement d’une bulle de gaz dans un liquide.” *La Houille Blanche*, 34, 31-42 (in French).

Culligan, K. A., Wildenschild, D., Christensen, B. S. B., Gray, W. G., and Rivers, M. L. (2006). “Pore-scale characteristics of multiphase flow in porous media: A comparison of air–water and oil–water experiments.” *Adv. Water Resour.*, 29(2), 227-238.

Ervine, D. A. (1998). “Air entrainment in hydraulic structures: A review.” *Proc. Instn Civ. Engrs, Water, Maritime & Energy*, 130(3), 142-153.

Falvey, H. T. (1980). “Air–water flow in hydraulic structures.” *Water and Power Resources Service*, Engineering Monograph, No. 41.

Falvey, H. T., and Ervine, D. A. (1988). “Aeration in jets and high velocity flows.” *Model-prototype correlation of hydraulic structures*, Colorado Springs, Colorado, 25-55.

Felder, S., and Chanson, H. (2014). “Air–water flows and free-surface profiles on a non-uniform stepped chute.” *J. Hydraul. Res.*, 512(2), 253-263.

Frizell, K. W., Renna, F. M., and Matos, J. (2013). “Cavitation potential of flow on stepped spillways.” *J. Hydraul. Eng.*, 139(6), 630-636.

Gameson, A. L. H. (1957). “Weirs and aeration of rivers.” *J. Inst. Water Eng.*, 11(5), 477-490.

Guo, J, Yang, S. Q., and Lim, S. Y., (1999). “Mechanism of energy transportation and turbulent flow in a 3D channel.” *J. Hydraul. Eng.*, 125(3), 684-692.

Guo, Y. K. (2014). “Numerical simulation of the spreading of aerated and nonaerated turbulent water jet in a tank with finite water depth.” *J. Hydraul. Eng.*, 140(8), 04014034.

Haberman, W. L., and Morton, R. K. (1954). “An experimental study of bubbles moving in liquids.” *Trans. ASCE*, 2799, 227-252.

Hager, W. H. (1991). “Uniform aerated chute flow.” *J. Hydraul. Eng.* 117(4): 528-533.

Kobus, H. (1991). “*Introduction to air-water flows*.” IAHR Hydraulic Structure Design Manual No. 4, Hydraulic considerations, Editor by Wood I. R., Balkema Publishers, Rotterdam, the Netherlands.

Kramer, K. (2004). “*Development of aerated chute flow*.” Ph.D. thesis, ETH, Zurich.

Liang, Z. C., and Wang, D. Z. (1982). "On the air carrying capacity in turbulent boundary layer." *Shuili Xuebao*, 2, 24-31 (in Chinese).

Medwin, H., Kurgan, A., and Nystuen, J. A. (1990). "Impact and bubble sound form raindrops at normal and oblique incidence." *J. Acoust. Soc. Am.*, 88(1), 413-418.

Oguz, H. N., and Prosperetti, A. (1990). "Bubble entrainment by the impact of drops on liquid surfaces." *J. Fluid Mech.*, 219, 143-179.

Pagliara, S, Carnacina, I, and Roshni, T. (2011). "Inception point and air entrainment on flows under macroroughness condition." *J. Environ. Eng.*, 137(7), 629-638.

Pfister, M., and Hager, W. H. (2011). "Self-entrainment of air on stepped spillways." *Int. J. Multiphase Flow*, 37(2), 99-107.

Pfister, M., and Chanson, H. (2014). "Two-phase air-water flows: Scale effects in physical modeling." *J. Hydrodyn.*, 26(2), 291-298.

Pumphrey, H. C., and Bjørnøl, C. L. A. (1989). "Underwater sound produced by individual drop impacts and rainfall." *J. Acoust. Soc. Am.*, 85, 1518-1526.

Rein, M. (1998). "Turbulent open channel flows: drop-generation and self-aeration." *J. Hydraul. Eng.*, 125(1), 98-102.

Straub, L. G., and Anderson, A. G. (1958). "Experiments on self-aerated flow in open channels." *J. Hydraul. Div.*, 84(7), 1-35.

Strotos, G., Malgarinos, I., Nokolopoulos, N., and Gavaises, M. (2016). "Predicting droplets deformation and breakup for moderate Weber numbers." *Int. J. Multiphase Flow*, 85, 96-109.

Toombes, T., and Chanson, H. (2007). "Surface waves and roughness in self-aerated supercritical flow."

Environ. Fluid Mech., 7(3), 259-270.

Valero, D., and Bung, D. B. (2016). "Development of the interface air layer in the non-aerated region of high-velocity spillway flows. Instabilities growth, entrapped air and influence on the self-aeration onset." *Int. J. Multiphase Flow*, 84, 66-74.

Valero, D., and Bung, D. B. (2018a). "Reformulating self-aeration in hydraulic structures: Turbulent growth of free surface perturbations leading to air entrainment." *Int. J. Multiphase Flow*, 100, 127-142.

Valero, D., and Bung, D. B. (2018b). "Artificial Neural Networks and pattern recognition for air-water flow velocity estimation using a single-tip optical fibre probe." *J. Hydro-Environ. Res.*, 19, 150-159.

Valero, D. (2019). "*On the fluid mechanics of self-aeration in open channel flows*." Ph.D. thesis, University of Liège, Belgium.

Volkart, P. (1980). "The mechanism of air bubble entrainment in self-aerated flow." *Int. J. Multiphase Flow*, 6, 411-423.

Wang, S. K., Lee, S. J., Jones, O. C., and Lahey, R.T. (1990). "Statistical analysis of turbulent two–phase pipe flow." *J. Fluids Eng.*, 112(3), 89-95.

Wilhelms, S. C., Gulliver, J. S., Ling, J. T., and Ling, R. S. (2005). "Gas transfer, cavitation and bulking in self-aerated spillway flow." *J. Hydraul. Res.*, 43(5), 532-539.

Wei, W. R., Deng, J., and Liu, B. (2013). "Influence of aeration and initial water thickness on axial velocity attenuation of jet flows." *J. Zhejiang Univ. SC. A*, 14(5), 362-370.

Wei, W. R., Deng, J., and Zhang, F. X. (2016). "Development of self-aeration process for supercritical chute flows." *Int. J. Multiphase Flow*, 79, 172-180.

Wood, I. R. (1984). “Air entrainment in high speed flows.” *Proc. of the Intl. Symp. on Scale Effects in Modelling Hydraulic Structures*, IAHR, Paper 4.1, IAHR Hydraulic Structure Design Manual Balkema Publishers, Rotterdam, the Netherlands.

Wood, I. R. (1991). “*Free surface air entrainment on spillways*.” IAHR Hydraulic Structure Design Manual No. 4, Hydraulic considerations, Editor by Wood I. R., Balkema Publishers, Rotterdam, the Netherlands.

Xi, R. Z. (1988). “Characteristics of self-aerated flow on steep chutes.” *In Proc. Symp. on Hydraulics for High Dams*, *IAHR*, Beijing, China.

Xu, W. L., Deng, J., Qu, J. X., Liu, S. J., and Wang, W. (2004). “Experimental investigation on influence of aeration on plane jet scour.” *J. Hydraul. Eng.*, 130(2), 160-164.

Xu, W. L., Luo, S. J., Zheng, Q. W., and Luo, J. (2015). “Experimental study on pressure and aeration characteristics in stepped chute flows.” *Sci. China Technol. Sc.*, 58(4), 720-726.

Yang, S., and Dou, G. (2010). “Turbulent drag reduction with polymer additive in rough pipes.” *J. Fluid Mech.*, 642, 279-294.

Yuan, Y. Z., and Xiang, J. J. (1988). “Motion of gas bubbles downstream aeration ramp.” *J. Hohai Univ.*, 16(1), 26-33 (in Chinese).

(a) **(b)**

Fig. 1. Air–water flows in hydraulic engineering: (a) Jinping-I dam; (b) Wudu spillway (photos taken by Professor Jun Deng).

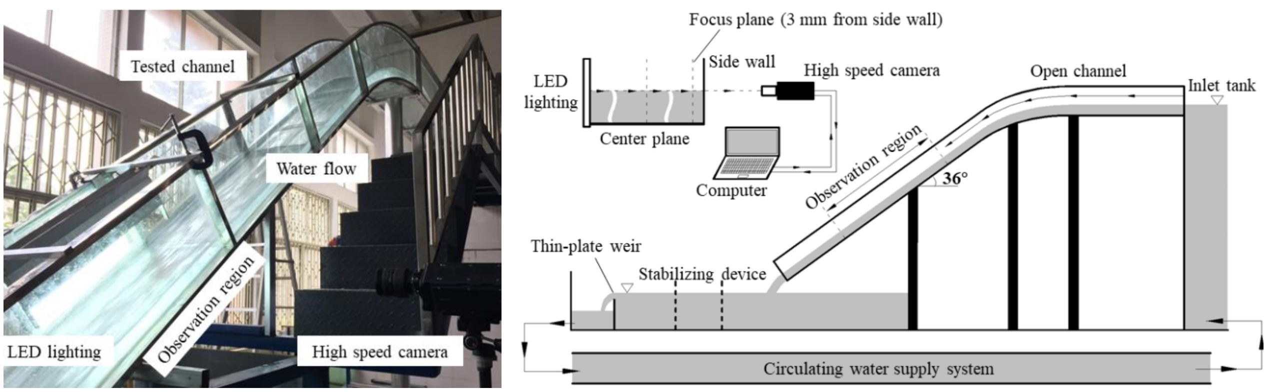

(a) **(b)**

Fig. 2. Experimental facility and arrangement: (a) experimental flume photo; (b) observation arrangement.

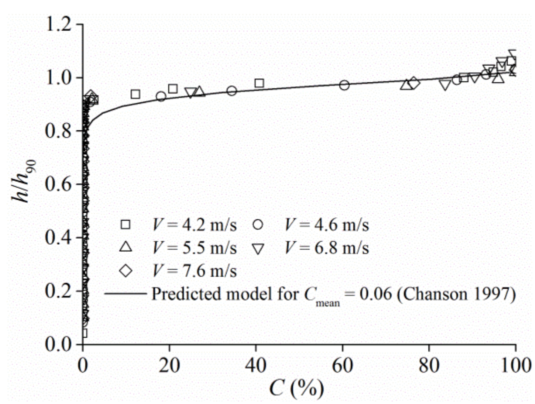

Fig. 3. Air concentration profiles at observation regions.

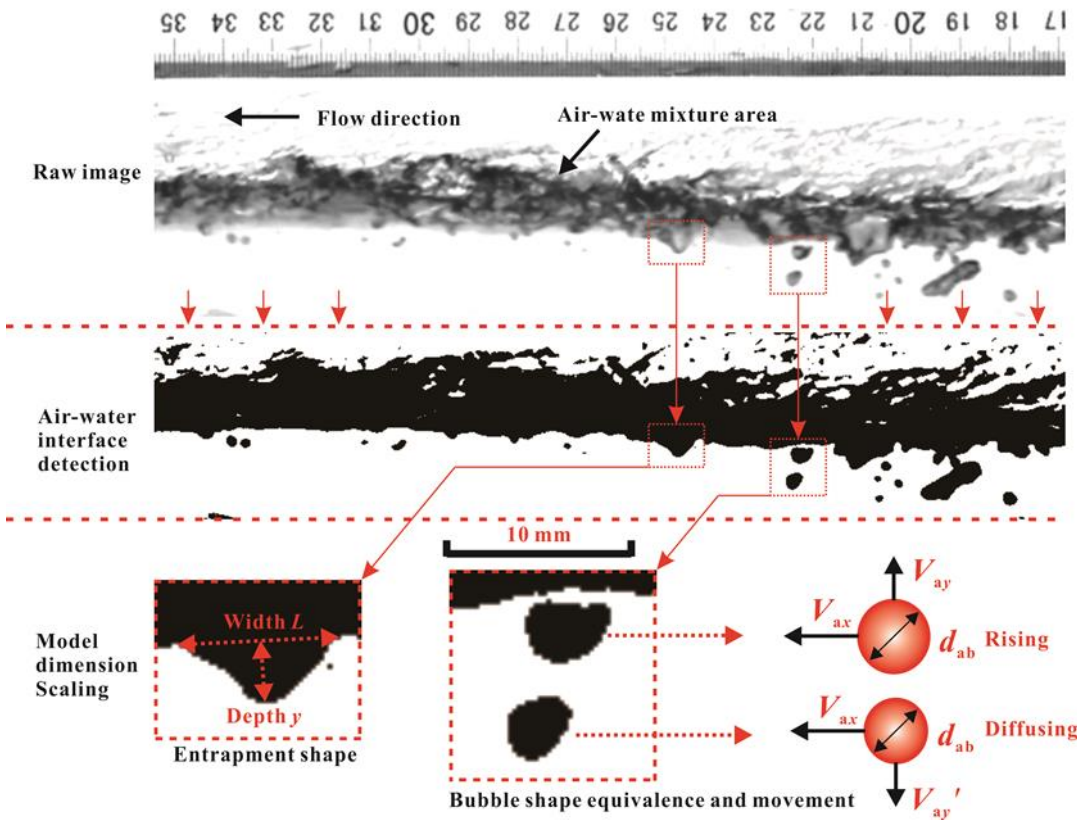

Fig. 4. Image processing for air–water interface and bubble size scales.

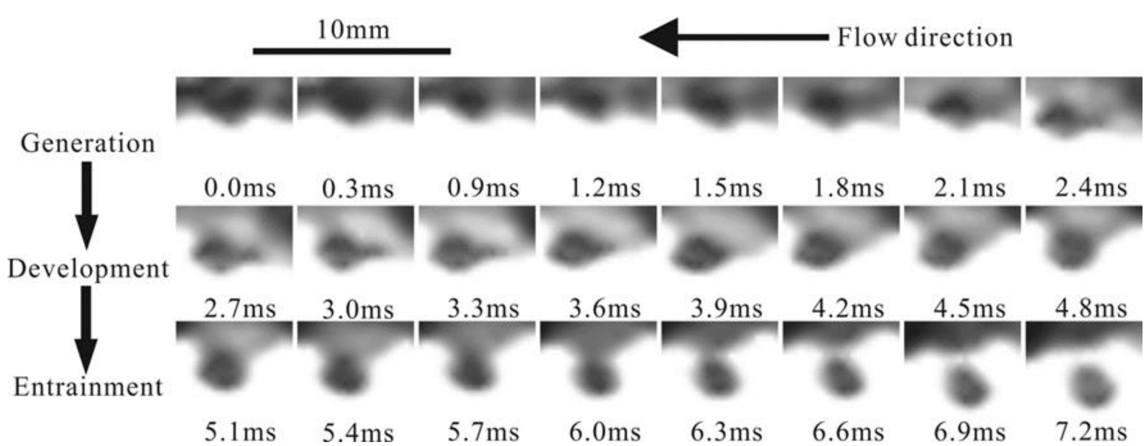

Fig. 5. High speed images of the free surface deformation and bubble entrainment for V = 5.5 m/s. Grey-dark shade represents air and white represents water.

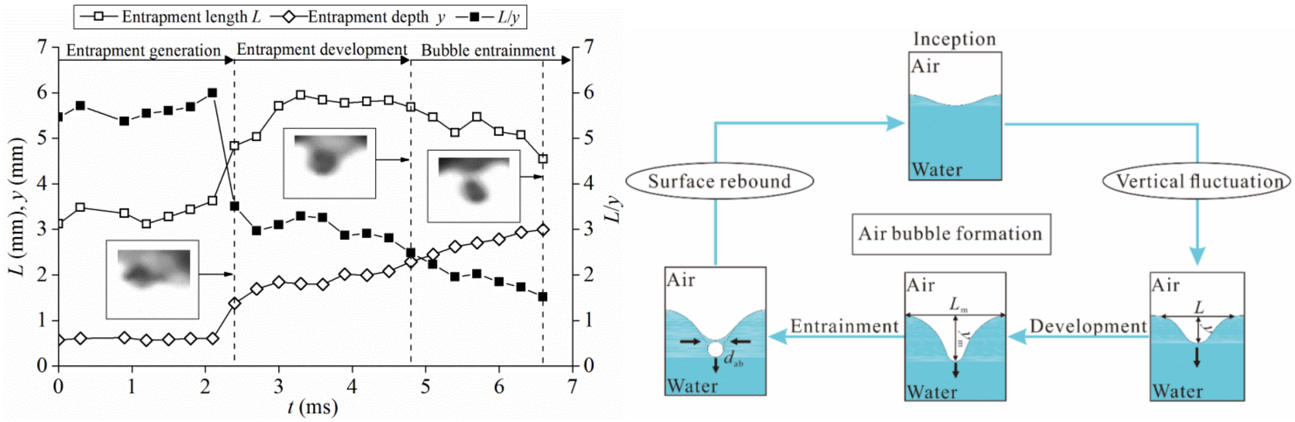

(a) **(b)**

Fig. 6. Size scale and entrapped shape variations over time of (a) observation for $V = 5.5$ m/s and $Re = 2.97\times10^5$ and (b) schematic diagram showing the processes for bubble formation.

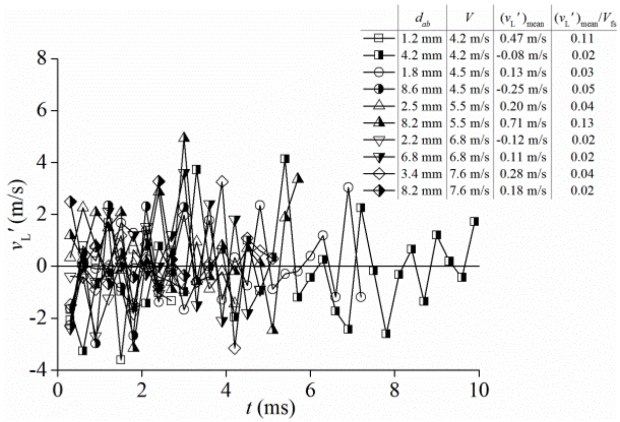

(a)

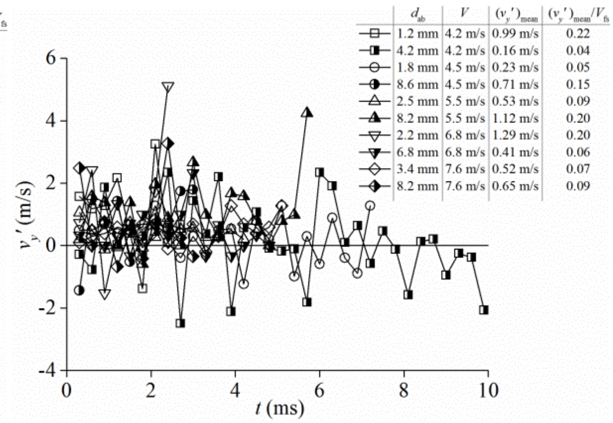

(b)

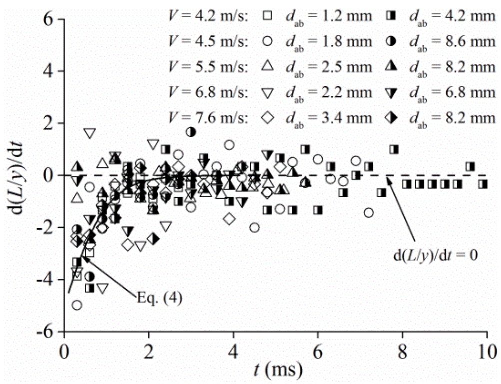

(c)

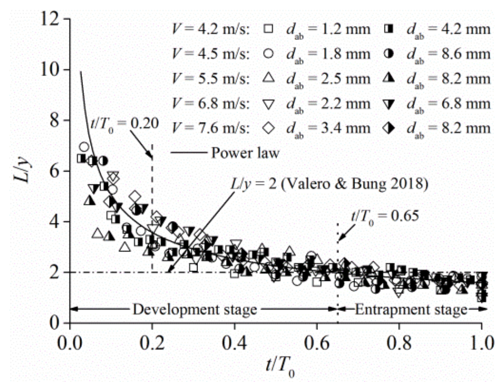

(d)

Fig.7. Geometry deformation with time for different bubble size generations: (a) entrapment length; (b) entrapment depth; (c) ratio of length to depth; (d) shape variations with dimensionless time.

553

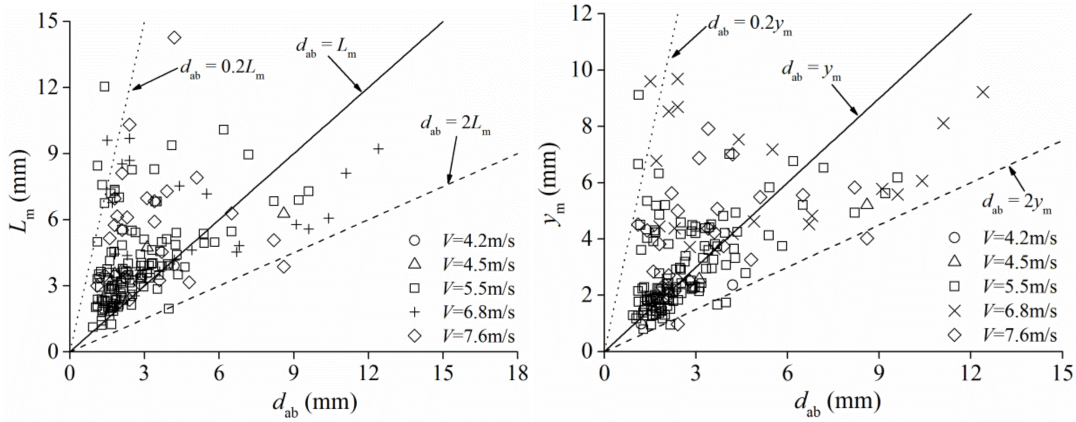

(a) **(b)**

Fig. 8. Relation of (a) entrapped width and (b) depth scale with the entrained bubble size scale.

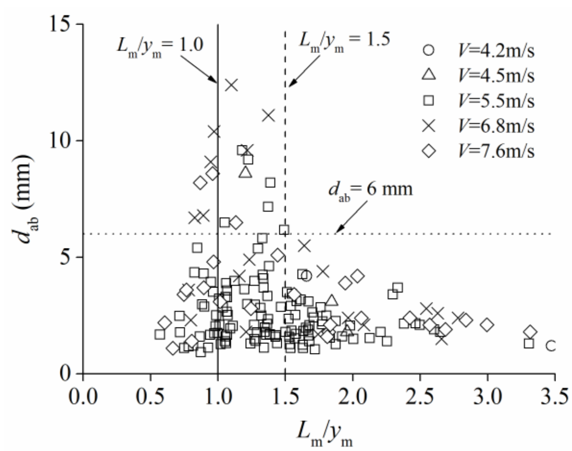

Fig. 9. Effect of entrapped shape on entrained bubble size scale.

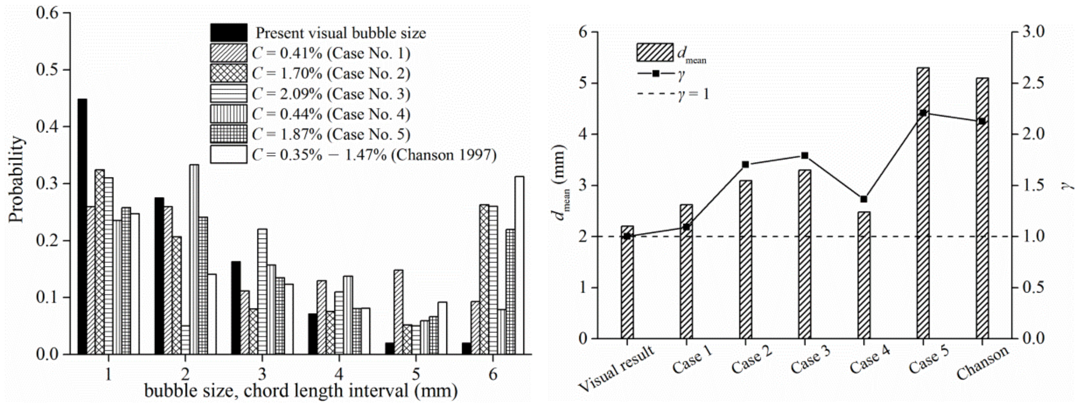

(a) **(b)**

Fig. 10. Comparison of observed bubble size generation with intrusive measurements of bubble chord length: (a) bubble size distribution; (b) average bubble size.

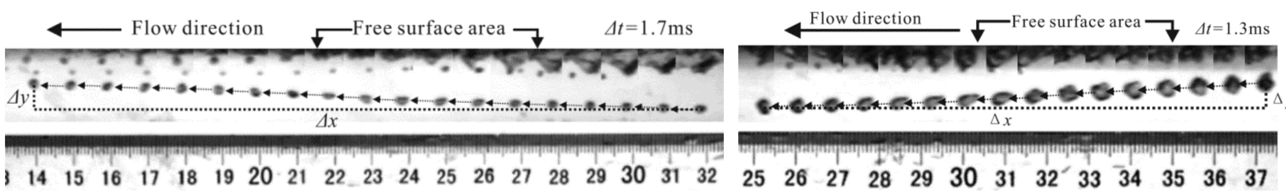

(a) **(b)**

Fig. 11. Single bubble (a) rising (d_{ab} = 3.0 mm) and (b) penetration (d_{ab} = 4.5 mm) processes in the water flow (V = 5.5 m/s).

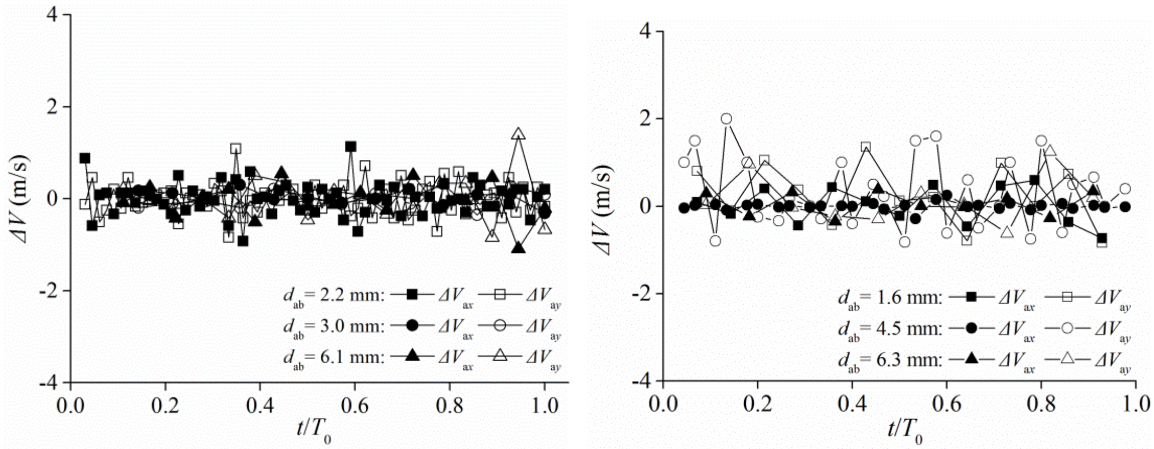

(a) **(b)**

Fig. 12. Time variation of velocity fluctuation in longitudinal ($\varDelta V_{ax}$) and vertical ($\varDelta V_{ay}$) direction for (a) rising and (b) penetration processes (V = 5.5 m/s).

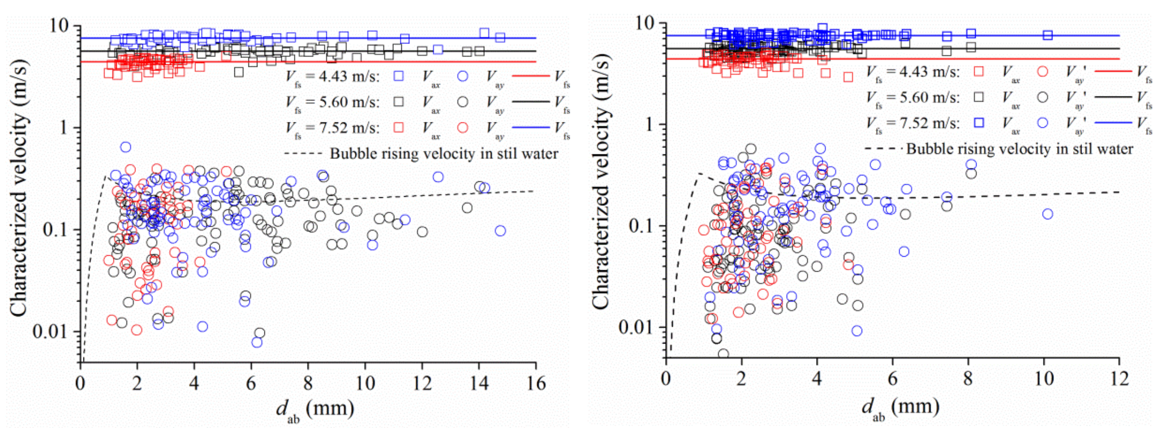

(a) **(b)**

Fig. 13. Characterized velocities of different bubble sizes for (a) rising and (b) penetration processes.

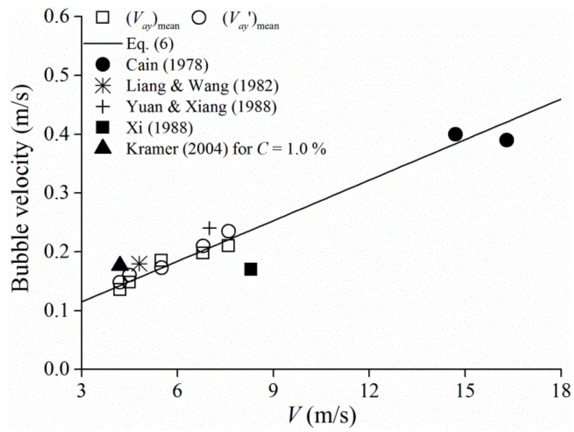

Fig. 14. Effect of flow velocity on characteristic bubble velocities in open channel flows.

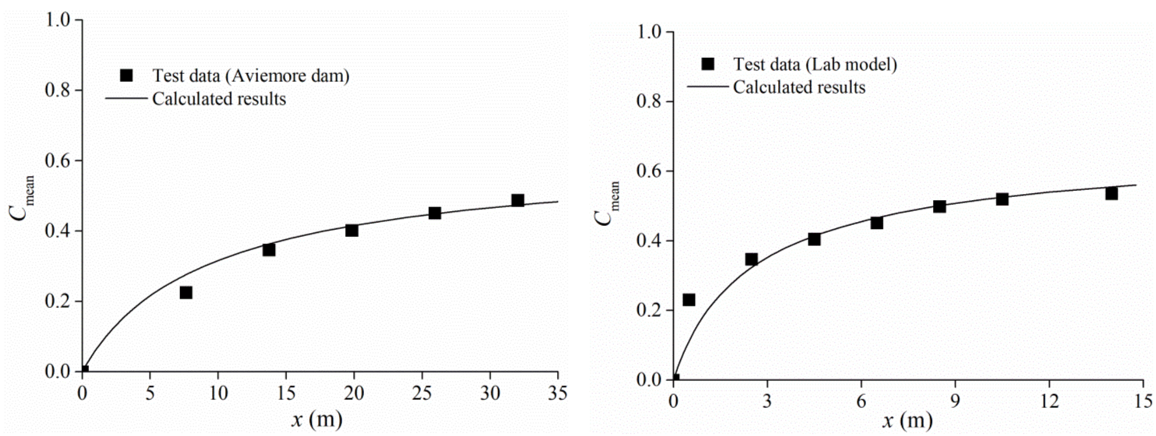

(a) **(b)**

Fig. 15. Comparison of calculated results with Eq. (6) to test data on C_{mean} variations along the air–water open channel flows: (a) Aviemore dam, prototype (Cain 1978); (b) Laboratory experiment (Xi 1988).

Table 1. Test Program and Flow Parameters.

Case No.	V (m/s)	Q (m^3/s)	C_{mean} (-)	V_{fs} (m/s)	Re ×10^5(-)
1	4.2	0.109	0.061	4.43	2.73
2	4.5	0.117	0.074	4.82	2.93
3	5.5	0.119	0.067	5.60	2.97
4	6.8	0.131	0.079	6.58	3.26
5	7.6	0.137	0.056	7.52	3.42

Table 2. Comparison of Characterized Bubble Velocities with Literature in Open Channel Flows.

No.	Case	V (m/s)	V_r from test inference (m/s)	V_r from Eq. (6) (m/s)
1	Cain (1978) Prototype spillway on Aviemore dam, deduced by Chanson (1993)	14.7	0.40	0.38
		16.3	0.39	0.42
2	Yuan & Xiang (1988) Laboratory chute test	7.6	0.24	0.22
3	Liang & Wang (1982) Laboratory chute test	4.8	0.18	0.16
4	Xi (1988) Scaled Model spillway on Meishan dam, deduced by Chanson (1993)	8.3	0.17	0.24
5	Kramer (2004) Laboratory chute test for C = 1.0%	4.2	0.18	0.14